Supporting Information for

Bifurcation instructed design of multistate machines

Teaya Yang, David Hathcock, Yuchao Chen, Paul McEuen, James P. Sethna, Itai Cohen and Itay Griniasty

Itay Griniasty.
E-mail: griniasty@cornell.edu

This PDF file includes:

Other supporting materials for this manuscript include the following:

Movies S1 to S2

Supporting Information Text

Contents

1. Calculation of the potential energy landscape

To model the dynamics of our experimental hinge system, we compute the potential energy landscape arising from the dipole-dipole interactions between the magnets embedded in each panel. The magnets used in our experiments are well approximated by perfect dipoles. Therefore, the potential energy for the system is a sum of dipole-dipole interaction energies

$$V = -\sum_{i\in P1}\sum_{j\in P2}\frac{\mu_0 m^2}{4\pi|\mathbf{r}_{ij}|^3}\left[3(\hat{\mathbf{m}}_i\cdot\hat{\mathbf{r}}_{ij})(\hat{\mathbf{m}}_j\cdot\hat{\mathbf{r}}_{ij})-\hat{\mathbf{m}}_i\cdot\hat{\mathbf{m}}_j\right], \quad [1]$$

where μ_0 is the vacuum permeability, m is the dipole strength (identical for all magnets), $\mathbf{m}_i$ is the orientation of dipole i, and $\mathbf{r}_{ij}$ is the distance between magnets i and j. Note that the interaction energy for dipoles in the same panel is constant, so we can restrict the sum to pairs of dipoles in different panels.

To derive the θ dependence of the energy landscape, we must write the dipole orientations and positions in terms of our control parameters x, y, and z and the dynamical variable θ. The dipoles on panel P1 are always oriented in the z-direction, while the dipoles on the rotating panel P2 have orientation that changes with θ:

$$\begin{aligned}\hat{\mathbf{m}}_i &= \delta_i\hat{\mathbf{z}}\\ \hat{\mathbf{m}}_j &= \delta_j\{\sin\theta\,,\,0,\,-\cos\theta\},\end{aligned} \quad [2]$$

where $\delta_i = \pm 1$ is the orientation of magnet i with respect to panel P1 (similar for δ_j). The positions of individual dipoles are given by

$$\begin{aligned}\mathbf{r}_i &= \{x_i, y_i, 0\} + \{x, y, z\}\\ \mathbf{r}_j &= R_\theta\{x_j, y_j, 0\},\end{aligned} \quad [3]$$

leading to interdipole distance $\mathbf{r}_{ij} = \mathbf{r}_i - \mathbf{r}_j$. Here x_i and y_i are the $x-y$ positions of dipole i in panel P1 (similar for x_j, y_j), x, y, and z are the coordinates of the control panel, and R_θ is the rotation matrix corresponding to a rotation by angle θ about the y-axis.

Together Eqs. (1-3) give the potential energy in terms of the hinge angle θ, our control parameters x, y, and z, and design parameters x_i, y_i, δ_i, x_j, y_j, and δ_j. Since the hinge experiment is heavily damped, θ follows gradient dynamics $\dot{\theta} = \partial_\theta V$ and the stable equilibrium angles are given by the local minima of the potential landscape V.

2. Cusp experiments

In the cusp experiments, panel P1's x and y positions are measured as displacements from their value when the panels are 180° open, and are aligned along z and y axes such that the panel's backs and bottoms are parallel. The magnets closest to the hinge axis are removed from it by 0.75cm on both panels. The back of the cylindrical magnets are aligned with the panel's backs. The damping paddle used in the cusp experiments have dimensions 1.5cm by 3.0cm.

A. Experimental estimation of the cusp point. We estimate the location of the cusp point as the intersection of the two measured saddle-node curves. We map the saddle-node curve by toggling x (y), for a given value of y (or x), so that the system snaps back and forth, and record the values of the control parameters x and y, and θ immediately after each transition (Fig. S2). Moreover, to verify the position of the cusp we record the angle θ of the system before and after snapping, and observe that the change in angle upon snapping disappears at the cusp point.

Finally, we inspect all data collected along the bifurcation curves as shown in Fig. 2a in the main text, and use a spline fit for the saddle-node bifurcations from L to S and the saddle-node bifurcations from S to L. We define the cusp point as the intersection of the two splines.

B. Single snap experiment. The mangeto elastic potential calculated for the experiment predicts a cusp at a slightly removed parametric position. The discrepency between the experimentally measured and theoretically predicted cusps could be due to fabrication errors. To effectively compare theory and experiment in this section only, we parameterize the system as a function of its displacement from the cusp for both theory and experiment using using dx and dy. We then follow the predicted path by controlling panel P1's x and y positions using the translation stages. We begin the experiment by letting the system maintain its equilibrium at the initial dx, dy position. We then change the position of panel P1 at a slow and steady rate. Angle measurements are recorded at various locations in the loop as shown in Fig. S1(a) (see also Fig. 1 in the main text), and the change in position is paused once the transition happens at point vi in order to let the system settle down and obtain an accurate angle measurement. We confirm that the system returns to its original state once we return to the starting dx, dy position.

C. Scaling experiment. To fit the scaling relations, we use the the same section of the data set used for determining the location of the experimental cusp point. We neglect data in the nonlinear region of the saddle-node curves far away from the cusp point, as well as data too close to the cusp point, where the errors due to measurement noise are comparable to the distance to the cusp. The data points used for the scaling relations are highlighted in Fig. S2(a). The state parameter values used in the scaling analysis correspond to the angle measurements obtained at the points right after the snap through transitions.

3. One dimensional bifurcations of equilibria

A. Normal form scaling and lever advantage. The ability to design magneto elastic machines and control parameter pathways that robustly lead to complex actions corroborates the validity of a new design paradigm: operation near bifurcations of multiple equilibria. The demonstrated trajectories take advantage of the structure of available dynamics near bifurcations of equilibira. These bifurcations are the loci of multiple distinct coalescing saddle-node manifolds, as illustrated for the idealized symmetric butterfly bifurcation (Fig. 3b in the main text). By weaving a trajectory that crosses and avoids chosen saddle-node bifurcations, we design a pathway that leads to complex actions. The system then cycles through multiple states via small variations of the control parameters, taking advantage of the multiple accessible lever mechanisms associated with these saddle-node surfaces. The sensitivity of the realized design increases as the number of equilibria associated with the bifurcation grows.

Butterfly, cusp and saddle-node bifurcations are the first in a series of bifurcations of equilibria in one-dimensional gradient systems. More generally, in systems with a single degree of freedom θ, bifurcations of k equilibria are points in parameter space where the first k derivatives of the potential vanish, $\{dV/d\theta, d^2V/d\theta^2, \ldots, d^kV/d\theta^k\} = \vec{0}$. That is, they are equilibrium points satisfying $k-1$ equations beyond that of mechanical equilibrium $dV/d\theta = 0$ and therefore lie on a manifold of co-dimension $k-1$ within the equilibrium manifold. The sensitivity of a bifurcation of k equilibria to variation in its parameters can be estimated through the topological equivalence of the dynamics near it to those in a normal form potential

$$\widetilde{V} = \varphi^{k+1} + \sum_{i=1}^{k-1} a_i \varphi^i, \qquad [4]$$

where the variable $\varphi(\theta)$ and normal form parameters $a_i(p)$ are coordinate transformations of the angle θ and parameters p respectively. The normal form describes the unfolding of the Taylor expansion of the potential at the bifurcation $V \sim \theta^{k+1}$ by variations of the parameters (1–3). The unfolded normal form potential demonstrates that the parameteric environment of a codimension k bifurcation includes domains with 1 to $\lceil (k+1)/2 \rceil$ minima delineated by k saddle-node manifolds which coalesce at the bifurcation. Moreover, it implies scaling relations between the variation in the system's state upon a snap through transition induced by crossing a saddle-node bifurcation associated with a codimension $k-1$ bifurcation and the variation of a normal form parameter that causes the snap:

$$\delta\varphi \propto a_m^{1/(k-m+1)}, \quad m < k-1. \qquad [5]$$

Heuristically the scaling can be derived from the normal form by noting that near the bifurcation the k^{th} derivative of the potential must still vanish, and so $\delta\varphi^2 \sim a_{k-1}$. Similarly the next $k-1$ derivatives must progressively vanish, setting the scaling of a_m. Thus the system state response to a general small perturbation scales at the very least as a square root of the variation of the normal form parameters. Furthermore, these scaling relations can be used to relate the magnitudes of the normal form coefficients on the saddle surfaces where snap-transitions occur. In terms of the leading coefficient we have,

$$a_m \sim a_{k-1}^{(k-m+1)/2}. \quad [6]$$

An explicit proof of these relations is given in (4) and summarized in (5, Sec. 36.6). These scaling relations carry over to the original variable and parameters near the bifurcation where the maps $\varphi(\theta)$ and $a_m(p)$ are approximately linear. Indeed, the scaling relations we experimentally observed near a the cusp bifurcations are those of the systems state with the normal form parameters near a bifurcation of three equilibria, i.e., a cusp (4, 5).

These scaling relations imply that the sensitivity of the system to variations of parameters grows exponentially with the number of associated equilibria. A system designed near a bifurcation of k equilibria can toggle its state between order unity separated states, $\delta\varphi \sim 1/2$, in response to variations of the linear normal form coefficient a_1 of order $1/2^k$. That is, both the potential lever advantage and the sensitivity to noise in the parameters grow as the number of associated equilibria grows. However, the parametric domain in which the mapping to the normal form is linear is often very small. The nonlinearity of the mapping often blunts the sensitivity of the response. Thus, the increased lever advantage near bifurcations of multiple equilibria is often not experimentally accessible. Conversely the system is not so sensitive to parametric noise when operated at a small parametric distance from the bifurcation about which it is designed, as demonstrated by the reproducibility of the experimental three state system, which was easily constructed twice.

B. Controlling a bifurcation instructed machine with only a few parameters. The number of control parameters required to unfold a bifurcation of n equilibria is naively $n-1$. However, implementing so many controls might be unfeasible in many scenarios. We propose here a theoretical design strategy where by employing only 3 control parameters a machine designed near a bifurcation of n equilibria can transition between its associated states.

To unfold a bifurcation of n equilibria with only 2 parameters, first design the system to operate near the Chebyshev polynomial of the first kind $T_n(x)$ associated with it, which oscillates between n minima and maxima with potential wells of equal depth. Then allow 2 parameters to change the first and second polynomial coefficients i.e. the potential $V(x) \approx ax + bx^2 + T_n(x)$. One can solve analytically for the values of a and b on the saddle-node surfaces:

$$a = \frac{n\left(n\,x\,T_n(x) + \left(1-2x^2\right)U_{n-1}(x)\right)}{x^2-1}, \quad b = \frac{n(x\,U_{n-1}(x) - n\,T_n(x))}{2\,(x^2-1)}.$$

Where $U_n(x)$ is a Chebyshev polynomial of the second kind. This gives a two dimensional unfolding similar to that of the symmetric butterfly, which allows transitions between any pair of states. Most parametric controls will allow access to the first and second polynomial coefficients of the potential (for example an external magnetic field has direct control of the linear coefficient in magnetic systems), however generally they also change other coefficients as well. Control of 3 parameters is likely to allow access to a perturbed version of this structure, and allow the system to transition between any pair of states. A downside to this strategy is that a such Chebyshev polynomials require either that the polynomial coefficients grow exponentially with the number of equilibria or that the potential well depth decays exponentially in the same manner. The design of a potential next to a Chebyshev polynomial is a formidable task for a system with generic interactions, as it requires that the higher order terms in the potential are negligible, and so also need to be tuned. These higher order terms might die away without tuning them in systems with polynomial interactions such as mechanical springs. To conclude, this strategy offers a trade-off between the number of controls and the depth of the potential barriers and the design complexity. Future investigation might offer strategies that circumvent this tradeoff, by allowing the depth of the potential wells to vary. Effectively, this is the approach we have experimentally implemented in the butterfly section of the manuscript.

C. Work scaling. Beyond the lever advantage, we can also derive a scaling law for the work done by the hinge as it snaps between equilibria. For this calculation, we assume that we sweep the control parameters adiabatically so that the system is instantaneously in equilibrium $\varphi^*(\{a_i\})$ and the rotational force (perpendicular to the panel) is zero, $F(\varphi^*) = -d\widetilde{V}/d\varphi|_{\varphi=\varphi^*} = 0$ This means that all the work is done during the snaps. The control mechanisms (which we do not explicitly model) store energy in the system by tuning it toward a saddle surface, then the snap in system state upon crossing the saddle surface dissipates this energy and does work. Working in normal form coordinates, the work done in snapping between two distinct equilibria φ_1^* and φ_2^* is simply the potential difference between these states

$$W = \int_{\varphi_1^*}^{\varphi_2^*} F(\varphi)d\varphi = \widetilde{V}(\varphi_2^*) - \widetilde{V}(\varphi_1^*). \quad [7]$$

Using the scaling relations Eqs. (5) and (6) together with the normal form potential, we find the following scaling for the work in terms of the leading normal form coefficient,

$$W \sim a_{k-1}^{(k+1)/2}. \quad [8]$$

As mentioned in the main text, this relation leads to a trade-off between the lever advantage and the work done by snaps between distinct equilibria. While increasingly high-order bifurcations enable increasingly sensitive dependence of the system state on parameter variations, the corresponding work done by transitions between these states decreases with bifurcation order.

4. Continuation algorithms

To find bifurcations of multiple equilibria in the dynamics of our model system and to map out the saddle-node structure in the vicinity of the high-order point, we use a series of continuation algorithms. In one dimension, a codimension k bifurcation point is defined by the vanishing of the first k derivatives of the potential: $\partial_\theta^j V(\theta^*, \{\xi_i\}) = 0$ for $j = 1, 2, \ldots, k$. These constraints define a codimenion k manifold in the space of dynamical variables and parameters $(\theta^*, \{\xi_i\})$.

A. Traditional continuation. Standard continuation algorithms compute bifurcation curves by varying a small number of parameters, and then projecting onto the bifurcation manifold (1). For example, suppose we have found a co-dimension k bifurcation. This requires the first k derivatives of the potential vanish, fixing θ^* and $k-1$ parameters $\xi_1, \xi_2, \ldots, \xi_{k-1}$. Varying an additional parameter ξ_k produces a line emanating from our initial point $(\theta^*, \{\xi\}) = p$. The continuation algorithm maps out this line by (i) taking a step along the tangent vector $T_k(p)$ to the curve, which is the null-vector of the gradient of the first k derivatives of the potential $T_k(p) \equiv \left\{\vec{v} \in \mathbb{R}^{k+1} \,|\, \forall j \in (1, 2, \ldots, k),\, \vec{v} \cdot \nabla_{\theta,\xi_1,\xi_2,\ldots,\xi_k} \partial_\theta^j V = 0\right\}$ and (ii) correcting this step using a Newton-Raphson algorithm* to search perpendicular to the step for a point where the first k derivatives of the potential vanish. This approach can be used to progressively search for higher order bifurcation points. For example, a fixed-point can be continued until $\partial^2 V(\theta^*, \{\xi_i\})/\partial\theta^2$ vanishes, indicating a saddle-node bifurcation. Continuing the saddle-node can lead to a cusp bifurcation, which in turn might lead to a swallowtail bifurcation. In this way, progressively adding parameters and performing continuations of one-dimensional curves can lead toward high-codimension bifurcation points. Algorithm 1 shows a procedural outline of the standard continuation algorithm. Once we have found a high-order bifurcation point, we use this algorithm to map out the saddle-node surfaces nearby. The surfaces can in turn be used to design cycles in control parameters that cause the system to perform desired snapping transitions.

Algorithm 1 Traditional Continuation

procedure CONT($p_0, V, k; \varepsilon$) ▷ find p s.t. $\{\partial_\theta^j V|_p\}_{j=1}^{k+1} = \vec{0}$
Ensure: $\{\partial_\theta V, \ldots, \partial_\theta^k V\}|_{p_0} = \vec{0}$
  $p \leftarrow (p_0)$
  $\text{sgn}_0 \leftarrow \text{sgn}(\partial_\theta^{k+1} V)|_{p_0}$
  while $\text{sgn}(\partial_\theta^{k+1} V)|_p = \text{sgn}_0$ **do**
    $v \leftarrow T_k(p)$ ▷ compute null-space
    $p \leftarrow p - \varepsilon \cdot \text{sgn}_0 \cdot v/\|v\|$ ▷ step along null-space
    $p \leftarrow \text{Newton-Raphson}(\{\partial_\theta^j V\}_{j=1}^k, v^\perp, p)$ ▷ pseudo-arclength correction
  $p \leftarrow \text{Newton-Raphson}(\{\partial_\theta^j V\}_{j=1}^{k+1}, \text{span}(\theta^*, \xi_1, \ldots, \xi_k), p)$ ▷ final nonlinear correction

The standard continuation approach, however, has limitations for microscopic machine design. In particular, it has limited utility for finding the high-order bifurcation points near which our machine will operate. In our model system we have many free parameters, including the positions of each of the magnets embedded in the panels. Varying a given experimental parameter does not guarantee we will find the next order bifurcation point. Instead we want to vary many parameters simultaneously, which greatly improves the likelihood that a higher-order bifurcation point is contained within the search space and allows for a more efficient approach toward that point. We have developed a gradient continuation algorithm to carry out this multi-parameter search.

B. Design algorithm: Gradient continuation. The gradient continuation algorithm works as follows. Suppose we have N parameters ξ_i in our system, plus the degree-of-freedom θ. A point, p, where the first k derivatives of the potential vanish belongs to a co-dimension k manifold in the full $(N+1)$-dimensional augmented parameter space, composed of the equilibrium state and control parameters, $(\theta^*, \{\xi_i\})$. Starting from the point p, take a step along the gradient of the $k+1$ derivative of the potential $\nabla_{\theta,\xi_1,\xi_2,\ldots,\xi_N} \partial_\theta^{k+1} V$, projected onto the tangent surface to the manifold at p. The tangent surface is the null-space of the gradient of the first k derivatives of the potential†, $T_{k,N}(p) \equiv \left\{\vec{v} \in \mathbb{R}^{N+1} \,|\, \forall j \in (1, 2, \ldots, k),\, \vec{v} \cdot \nabla_{\theta,\xi_1,\xi_2,\ldots,\xi_N} \partial_\theta^j V = 0\right\}$. This procedure finds the step within the co-dimension k manifold that maximizes the change in $\partial_\theta^{k+1} V$, which we need to vanish in order to find the next order bifurcation. After the step, the algorithm performs a corrective Newton-Raphson search (6), constrained to the hyperplane $T_{k,N}^\perp(p)$ perpendicular to the null-space, which returns to the codimension k manifold on which the first k derivatives of the potential vanish. As in the standard continuation, this approach is repeated to progressively find higher order bifurcation points. A visualization of the gradient search algorithm, applied to the potential $V = \theta^6 + a_4\theta^4 + a_2\theta^2 + a_1\theta$, is shown in Fig. 3b in the main text.

*Newton-Raphson(f, Ω, p) (6) searches for the roots of the functions f over the space Ω starting at the point p.

†Notice that this algorithm uses all N parameters $\xi_1, \ldots, \xi_N$ to search for a codimension k bifurcation, while the standard continuation in the previous section only used k parameters $\xi_1, \ldots, \xi_k$. The null-space $T_{k,N}(p)$ has dimension $(N - k + 1)$.

Algorithm 2 Gradient Continuation

procedure GCONT($p_0, V, k; \varepsilon$) ▷ find p s.t. $\{\partial_\theta^j V|_p\}_{j=1}^{k+1} = \vec{0}$

Ensure: $\{\partial_\theta V, \ldots, \partial_\theta^k V\}|_{p_0} = \vec{0}$

$p \leftarrow p_0$

$\text{sgn}_0 \leftarrow \text{sgn}(\partial_\theta^{k+1} V)|_{p_0}$

while $\text{sgn}(\partial_\theta^{k+1} V)|_p = \text{sgn}_0$ **do**

$v \leftarrow \nabla_{(\theta,\{\xi\})} \partial_\theta^{k+1} V$ ▷ find gradient

$v \leftarrow \pi_{T_{k,N}(p)}(v)$ ▷ project v onto null space $T_{k,N}(p)$

$p \leftarrow p - \varepsilon \cdot \text{sgn}_0 \cdot v/\|v\|$ ▷ step along gradient

$p \leftarrow \text{Newton-Raphson}(\{\partial_\theta^j V\}_{j=1}^{k}, T_{k,N}^{\perp}(p), p)$ ▷ pseudo-arclength correction

$p \leftarrow \text{Newton-Raphson}(\{\partial_\theta^j V\}_{j=1}^{k+1}, \text{span}(\theta^*, \{\xi_i\}), p)$ ▷ final nonlinear correction

5. Butterfly experiments

A. Butterfly panels. In the butterfly experiments, panel P1's x, y and z positions are measured as displacements from their value when the panels are 180° open. The magnets closest to the hinge axis are removed from it by 2.5cm on both panels. The panels are aligned vertically, and the back of the cylindrical magnets on panel P1 are aligned with the center of the magnets on panel P2 in the z direction. This small change in magnet alignment (compared to the single snap experiment) is found to reduce the discrepancy between experiment and prediction. An illustration for the panels is shown in Fig. S3. The damping paddle has dimensions 8.0cm by 2.5cm for the butterfly experiments. The position of the magnets on panel P1 was changed such that the system operates next to a butterfly bifurcation, as specified in the main text and in the following sections.

B. Application of the continuation algorithm. To find an experimentally feasible path and magnetic pattern, we implement the continuation algorithm by first finding a butterfly point in parameter space, then validating the resulting pattern against known experimental constraints (e.g. we require physically realizable panel angles and magnet positions). Before each search using the continuation algorithm, we first randomly generate orientations of the 18 magnetic dipoles on the two panels. We also randomly select two magnets on panel P1 to be displaced from their lattice positions, by $(dx1, dy1)$ and $(dx2, dy2)$ respectively. The search algorithm is always initialized with the values $\{\theta, dx, dy, dz, dx1, dy1, dx2, dy2\} = \{1.1\text{rad}, 0.5\text{cm}, -0.25\text{cm}, 0, 0, 0, 0, 0\}$.

Next, we let the algorithm try to find a butterfly bifurcation point. If no butterfly point can be found, we repeat the initialization process and repeat the search with a new randomly generated magnetic pattern. The butterfly point corresponding to the pattern we used in our experiments is located at $\{\theta, dx, dy, dz, dx1, dy1, dx2, dy2\} = \{2.131\text{rad}, -0.355\text{cm}, -0.304\text{cm}, -0.824\text{cm}, 0.918\text{cm}, -0.698\text{cm}, -0.326\text{cm}, -0.486\text{cm}\}$.

If the butterfly point is found, we investigate the potential plots at various points in parameter space near the bifurcation point. Specifically, we offset one or more of the 6 search parameters by ± 0.2 and find the number of minima that exist between 0 to 180 degrees at each of these locations. The potential plots at locations with three minima are then inspected to decide the experimental feasibility of the pattern. Ideally, all three minima are at least 5 degrees apart, and the smallest minimum is at least 5 degrees (for $z = 0$) to prevent the panels from touching during experiment. We also look for patterns with large triple-minima regions, for example if three visibly deep minima can be observed when at least one parameter is changed by ± 0.5cm.

After an experimentally feasible pattern is discovered, we manipulate the three experimentally controllable parameters (x,y,z) continuously around the point with deepest triple minima and observe changes in our model of the potential landscape. The design of the control path is guided by visualization of the saddle-node surfaces mapped out using the standard continuation algorithm detailed above. Several paths are tested in the model to obtain the desired sequence of bifurcations and to optimize various properties of the transitions (e.g. the magnitude of the snaps and depths of the minima).

C. Experiments for trajectories near a butterfly point. We set up the experiment by laser-cutting the holes for magnets at the exact locations corresponding to the found $dx1$, $dy1$, $dx2$, $dy2$ values, which were 1.418cm, −0.273cm, −0.826cm, and −0.986cm respectively. We also add a translation stage to control panel P1's z position. We begin the experiment by following the exact coordinates provided by the theoretically designed path. In the event that a predicted transition cannot be seen using the predicted path coordinates (due to fabrication or calibration errors shifting the surface), we translate the system further from the original predicted path to determine a more robust path that may account for some shifting in coordinates due to experimental errors (for example see Fig. 4b in the main text). Once an experimental path is shown to demonstrate the predicted behavior with the desired number of state transitions, we record the locations for state transitions in experiment, and repeat the experiment while slowing down the rate of change in x,y positions near the transitions to give the system enough time to respond in the presence of large damping. Movie S1 and S2 show demonstrations of such paths with clear transitions. Those experiments show excellent qualitative agreement with the theoretically designed paths, although the locations at which transitions happen and the equilibrium angle of the panel are often shifted by a small amount due to experimental error.

D. Additional operation mode: double-snap trajectories. The intricate saddle-node surface structure near the butterfly bifurcation enables a variety of snapping behaviors with the same panel design, beyond the 3-state cycle presented in the main text. Here we present a second snapping sequence that was measured experimentally.

By using the same trajectory in parameter space as the three-snap sequence in the main text, but traversing the path in the reverse direction, we observe a two-snap sequence between small (S) and large (L) angles. Fig. S4a shows this trajectory together with the same saddle surfaces from Fig. 4a in the main text. The experimentally measured angles along this backward cycle are shown in Fig. S4b (see also Movie S2). Besides a minor systematic shift in the angles of the L state, we find excellent fidelity between the predicted and measured angles. The snapping transitions occur almost exactly at the predicted locations.

Our example trajectories demonstrate that the saddle-node structure in the vicinity of a butterfly bifurcation enables a great deal of flexibility in controlling state transitions of a mechanical system. For practical applications, further fine-tuning of the control trajectory can be used to optimize the system's behavior (e.g., the positions of the steady states and their lifetimes in the presence of environmental noise).

E. Reassembly and repeatability. As evidence of the system's robustness, its behavior survived a complete rebuilding. Panels P1 and P2 where replaced by a new set of panels and magnets. The panels where glued into their new positions. We estimate the positional and alignment errors at 1mm and 2 square degrees respectively. After reassembly, both forward and backward operation modes display the same sequence of transitions without additional calibration.

6. Generalizations: multidimensional bifurcations and supplemental scaling behaviours

A. Stopping conditions in higher dimensions. While our proof-of-concept experiment is limited to a hinge with a single degree of freedom (the opening angle), our approach and gradient continuation algorithm are straightforward to apply to systems with multiple degrees of freedom, e.g. a microscopic robot with multiple panels connected by elastic hinges. The cuspoidal bifurcations discussed in this paper also naturally appear in higher-dimensional gradient systems. However, the analytic criteria to classify them is somewhat more complicated: we can not simply search for points where higher order derivatives of the potential vanish. In this section we will discuss stopping criteria in higher dimensions, i.e. what quantities should we follow with the gradient continuation algorithm to search for bifurcations of increasing order?

With two or more degrees of freedom, a saddle-node bifurcation occurs when a fixed-point (stable or unstable) collides with a saddle point, resulting in mutual annihilation. This occurs when an eigenvalue of the Hessian of the potential $A_{ij} = -\partial_{\theta_i}\partial_{\theta_j} V$ crosses 0 (here θ_i are the dynamical variables). For the purposes of applying gradient continuation starting from a fixed point, it is therefore convenient to use $\det A$ as the stopping criteria, since the determinant vanishes when an eigenvalue does.

Near a saddle-node bifurcation, the state space can be decomposed (by the Center Manifold Theorem) into (i) the invariant center manifold emanating from the fixed point along the direction of the critical eigenvector (with eigenvalue 0) and (ii) a stable/unstable manifold on which the flows exponentially grow or decay (for the purposes of machine design we generally want only stable directions). Due to the vanishing eigenvalue, the dynamics on the center manifold are nonlinear at lowest order. These dynamics can be determined perturbatively by expanding the gradient of the potential, projecting onto the center manifold and enforcing the invariance of the center manifold (1). Higher-order bifurcations occur when the center manifold expansion coefficients vanish. For example, vanishing quadratic term indicates a cusp bifurcation, vanishing cubic term indicates a swallowtail, and so on. Thus these coefficients replace the higher-order derivatives of the potential as the stopping criteria in the gradient continuation algorithm. Below we give explicit expressions for these expansion coefficients.

Suppose we have an n-dimensional system $\theta \in \mathbb{R}^n$ that undergoes a saddle-node bifurcation at $\theta = 0$. Near this point, the dynamics can be expanded as follows,

$$\dot{\theta} = A\,\theta + F(\theta), \tag{9}$$

where A is the Hessian of the potential (which has a zero eigenvalue) and $F(\theta)$ collects all quadratic and higher-order terms in multilinear forms,

$$\begin{aligned} F(\theta) &= \frac{1}{2}B(\theta,\theta) + \frac{1}{6}C(\theta,\theta,\theta) + \frac{1}{24}D(\theta,\theta,\theta,\theta) + \mathcal{O}(||\theta||^5) \\ &= \frac{1}{2}\sum_{i,j=1}^{n} \left.\frac{\partial^2 F(\phi)}{\partial\phi_i\partial\phi_j}\right|_{\phi=0} \theta_i\theta_j + \frac{1}{6}\sum_{i,j,k=1}^{n} \left.\frac{\partial^3 F(\phi)}{\partial\phi_i\partial\phi_j\partial\phi_k}\right|_{\phi=0} \theta_i\theta_j\theta_k \\ &\qquad + \frac{1}{24}\sum_{i,j,k,l=1}^{n} \left.\frac{\partial^4 F(\phi)}{\partial\phi_i\partial\phi_j\partial\phi_k\partial\phi_l}\right|_{\phi=0} \theta_i\theta_j\theta_k\theta_l + \mathcal{O}(||\theta||^5). \end{aligned} \tag{10}$$

Let ψ and φ be the right and left eigenvectors corresponding to the zero eigenvalue: $A\psi = 0$ and $A^T\varphi = 0$. The projection of θ onto the center manifold $\vartheta = \varphi\cdot\theta$ has dynamics

$$\dot{\vartheta} = a_2\vartheta^2 + a_3\vartheta^3 + \mathcal{O}(\vartheta^4). \tag{11}$$

Following Kuznetsov, we derive the coefficients up to fourth order (third order is given in Ref. (1)),

$$\begin{aligned} a_2 &= \frac{1}{2}\varphi\cdot B(\psi,\psi) \\ a_3 &= \frac{1}{6}\varphi\cdot C(\psi,\psi,\psi) + \frac{1}{2}\varphi\cdot B(\psi,b_2) \\ a_4 &= \frac{1}{24}\varphi\cdot D(\psi,\psi,\psi,\psi) + \frac{1}{4}\varphi\cdot C(\psi,\psi,b_2) + \frac{1}{8}\varphi\cdot B(b_2,b_2) + \frac{1}{6}\varphi\cdot B(\psi,b_3), \end{aligned} \tag{12}$$

where

$$\begin{aligned} b_2 &= A_{su}^{-1}\Big(\psi[\varphi\cdot B(\psi,\psi)] - B(\psi,\psi)\Big) \\ b_3 &= A_{su}^{-1}\Big(\psi[\varphi\cdot C(\psi,\psi,\psi) + 3\varphi\cdot B(\psi,b_2)] + 3b_2[\varphi\cdot B(q,q)] - C(\psi,\psi,\psi) - 3B(\psi,b_2)\Big) \end{aligned} \tag{13}$$

and A_{su}^{-1} is the inverse of A restricted to the stable/unstable subspace (which doesn't have zero eigenvalues). As mentioned above, vanishing a_2 indicates a cusp, if a_3 also vanishes we have a swallowtail, and if all three coefficients are zero we have a butterfly. The vectors b_2 and b_3 describe the curvature of the center manifold in the full θ space, $\theta = q\vartheta + b_2\vartheta^2/2 + b_3\vartheta^3/6$. While these bifurcations are one dimensional (they occur on the one-dimensional invariant center manifold), the curvature of the center manifold as we move further from the bifurcation point could allow snapping between states with reasonable separation in multiple dimensions. In principle, this would enable machines to carry out work cycles near a butterfly bifurcation.

While the results of this section (and the main text) are formulated in terms gradient systems $\dot{\theta} = -\nabla V$, they do not rely on this structure. Indeed, cuspoidal bifurcations also appear in general non-gradient systems in n-dimensions $\dot{\theta} = G(\theta)$ for a

general velocity field $G : \mathbb{R}^n \to \mathbb{R}^n$. Near a saddle-node bifurcation, these dynamics can again be expanded in the form Eq. (9), where now A is the Jacobian of the velocity field G, $A_{ij} = dG_i/d\theta_j$ (which has a zero eigenvalue). Again the above stopping criteria along with our gradient continuation algorithm can be used to identify a butterfly bifurcation in the dynamics. In non-gradient systems, periodicly oscillating and even chaotic attractors are possible. Therefore, it must be checked that upon crossing a saddle surface, the system transitions to a new equilibrium state instead of a non-fixed-point attractor. With this caveat, our results generalize to all systems governed by dynamical systems with tuneable design and control parameters. On the other hand, these more complex attractors might also provide interesting targets for design of sophisticated machines.

B. Scaling for the Thom's seven: hyperbolic and elliptic umbilics. Beyond the quasi-one-dimensional bifurcations there are also cuspoidal bifurcations that are genuinely multidimensional. In two dimensions, for example, we have elliptic umbilic, hyperbolic umbilic, and parabolic umbilic catastrophes (these together with the four one-dimensional bifurcations saddle-node, cusp, swallowtail, and butterfly make up the Thom seven). Like the cusp and butterfly bifurcations, the unfolding of the normal form predicts and intricate saddle-surface structure describing how fixed-points and saddle-points come together and collide in the vicinity of the bifurcation point. These higher-dimensional bifurcations also obey advantageous scaling laws, relating the changes in state to the variation of control parameters. For example, the normal form potentials for the elliptic and hyperbolic umbilics are

$$\begin{aligned} V_{\text{elliptic}} &= \frac{\theta_1^3}{3} - \theta_1\theta_2^2 + a(\theta_1^2 + \theta_2^2) + b\theta_1 + c\theta_2 \\ V_{\text{hyperbolic}} &= \theta_1^3 + \theta_2^3 + a\theta_1\theta_2 + b\theta_1 + c\theta_2 \end{aligned} \qquad [14]$$

from which the follow scaling can be derived (4),

$$\delta\theta_1, \delta\theta_2 \sim a \quad b, c \sim a^2. \qquad [15]$$

Increasing the dimension further leads to even more cuspoidal bifurcations; these have been enumerated by Arnold using an ADE classification (7). While the search criteria for such bifurcations is increasingly complicated, they provide a rich design space for multi-component machines.

C. Reynolds number scaling. The magnetic decorations in our experiments are arranged in each panel about a square lattice with unit separation of 2.5cm. To explore over-damped, gradient dynamics, that are ubiquitous in microscopic mechanisms, the rotating panel is attached to a paddle moving through a glycerol bath. The results of our experiments then hold also for smaller systems in fluid with comparable kinematic viscosity. If the system is smaller by a factor $\Omega \ll 1$, the time Δt it takes our macroscopic over-damped system, of typical size L, to traverse an angular expanse $\Delta\theta$ is equal to the time it takes a microscopic system, of size ΩL to traverse the same angular expanse in the same liquid. This comes about because both the viscous drag force and the magnetic force between dipoles of magnetization M_1 and M_2, $F_{\text{Drag}} \sim L^2\dot{\gamma}$, $F_{\text{dipole}} \sim M_1M_2/R^4$, are quadratic in the typical system sizes. For over-damped dynamics this results in a length-scale independent strain-rate, $\dot{\gamma}$. The system is over-damped if its Reynolds number $\text{Re} = L^2\dot{\gamma}/\nu$, is smaller then 1, where ν is the fluid's kinematic viscosity. The Reynold's number of a miniaturized system is therefore smaller by a factor of Ω^2. Reducing the system's size can compensate for changes in the system's composition, such as embedding it in water rather than glycerol, or the growth of magnetic dipole strength density as the system size decreases.

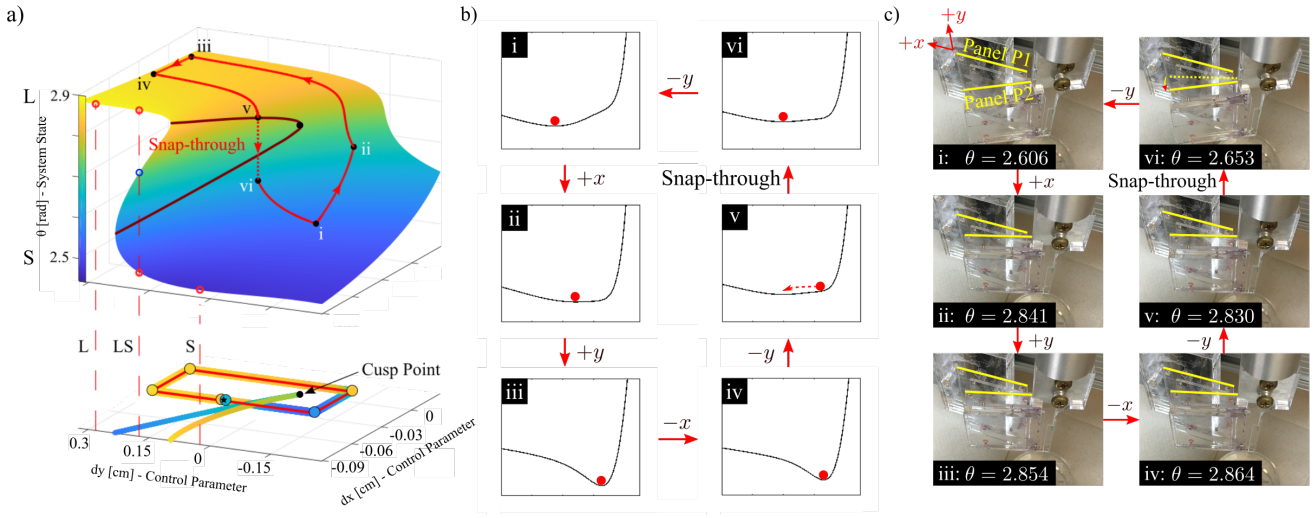

Fig. S1. Single snap-through mechanism (a.) As we vary the control parameters along a loop around the cusp point as shown, we expect to see a single snap-through buckling behavior (point v to point vi) for each cycle, akin to how hummingbirds use their beak to capture prey (8). **(b.)** The predicted potential energy curves for points labeled from i to vi are presented. The saddle-node bifurcation occurs between v and vi as indicated by the arrow in v. **(c.)** We experimentally observe the predicted snap-through behavior. Due to experimental errors, the location of the cusp point is shifted, but we see excellent agreement between the theory and measurements after shifting the coordinates to align the theoretical and experimental cusp points.

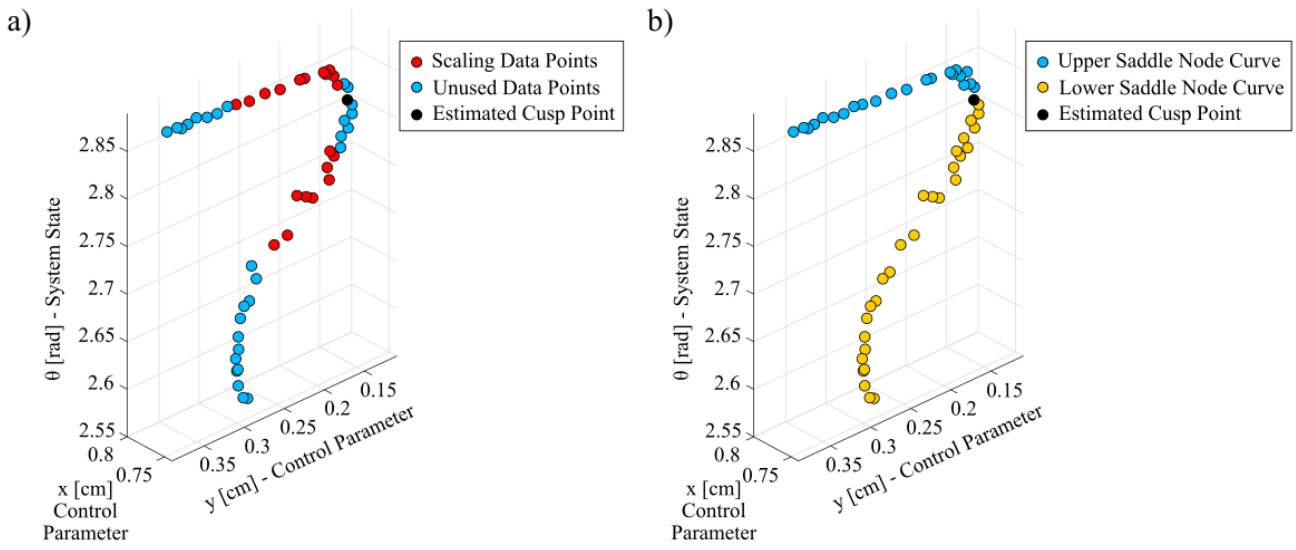

Fig. S2. Snap Through transitions near a cusp. These plots show the equilibrium angle recorded in experiments following a snap-through transition. The corresponding (x, y) denote the values of the control parameters at which the snap-through occurred. **(a.)** Highlights the the data points used to fit the cusp scaling. We exclude data far from the cusp, where higher order terms in the normal form are non-negligible, and close to the cusp, where measurement and fabrication error are comparable to the distance from the cusp. **(b.)** Highlights the data corresponding to the upper and lower saddle-node curves.

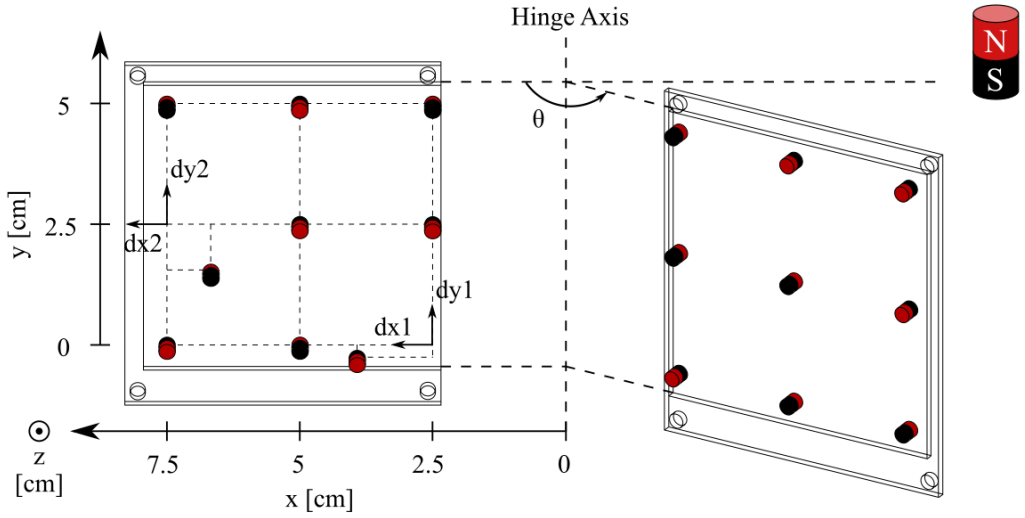

Fig. S3. Butterfly panels: In the butterfly experiments, panel P1's x, y and z positions are measured as displacements from their value when the panels are 180° open, the magnets closest to the hinge axis are removed from it by 2.5cm on both panels, the panels are aligned vertically and the back of the cylindrical magnets on panel P1 are aligned with the center of the magnets on panel P2. This small change in magnet alignment is found to reduce the discrepancy between experiment and prediction.

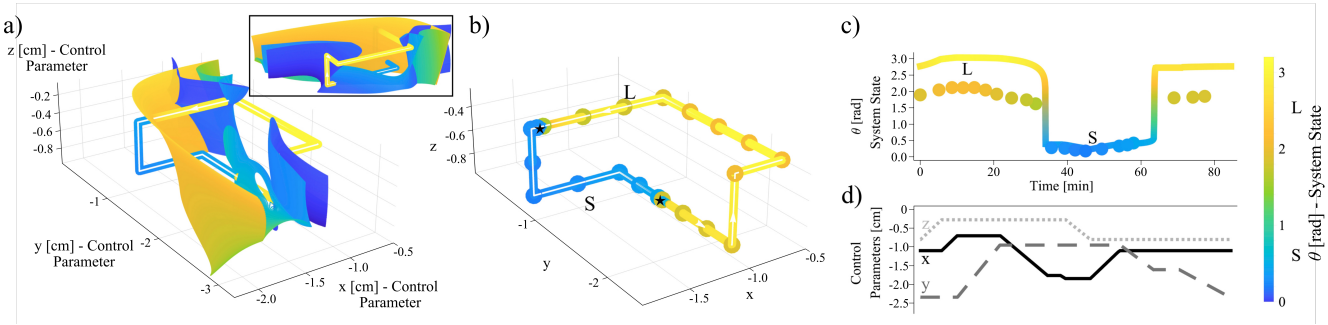

Fig. S4. 2-state Cycle Near Butterfly Bifurcation Point (a.) Theoretical design space: The saddle-node surfaces of a magneto-elastic system with three active control parameters, x,y and z are plotted, their color denotes the angle θ at which the snap occurs. The system's magnetic pattern is designed using the gradient continuation algorithm such that it operates near a butterfly bifurcation where multiple saddle-node surfaces coalesce, enabling multiple snap-through transitions at the surfaces. A trajectory (colored tube with white arrows) is chosen such that the system snaps in cycles between two states with Large (L) and Small (S) angles. This trajectory is identical to that for the 3-state cycle in Fig. 4 in the main text, but the path is traversed in the opposite direction. The system's predicted state is denoted by the tube's color. At intersections of the trajectory with a surface where their colors match the system is predicted to snap to a new state. The inset shows the same surface and trajectory from a different viewpoint (rotated by approximately $60°$). **(b.)** Experimental control trajectory: The colored disks mark the experimental measurements at various points along the designed trajectory. We observe two distinct transitions in the experiment (indicated by $\star$) as predicted. **(c.)** Experimental time series: Dots mark the measured system state, and the line represents the theoretically predicted system state as a function of the control parameters, which change according to the experimental control sequence. **(d.)** Experimental control sequence: Curves depict the variation of the control parameters, x, y and z as a function of time. **(Remark:)** Experiment and theory are also demonstrated in supplemental Movie S2.

Movie S1. Three state cycle near a butterfly bifurcation. An experimental demonstration of a system cycling between three states by snapping is accompanied by animations of the predicted elasto-magnetic potential and the system's trajectory in parameter space.

Movie S2. Two state cycle near a butterfly bifurcation. An experimental demonstration of a system snapping back and forth between two states. The system employs the same magnetic pattern near a butterfly bifurcation used to demonstrate transitions between three states. The experimental video is accompanied by animations of the predicted elasto-magnetic potential and the system's trajectory in parameter space.

References

1. Yuri A. Kuznetsov. Topological Equivalence, Bifurcations, and Structural Stability of Dynamical Systems. Springer New York, New York, NY, 2004. ISBN 978-1-4757-3978-7. . URL https://doi.org/10.1007/978-1-4757-3978-7_2.
2. John Guckenheimer and Philip Holmes. Nonlinear Oscillations, Dynamical Systems, and Bifurcations of Vector Fields. Springer New York, New York, NY, 1983. ISBN 978-1-4612-1140-2. . URL https://doi.org/10.1007/978-1-4612-1140-2_3.
3. J. W. Bruce and P. J. Giblin. Curves and Singularities: A Geometrical Introduction to Singularity Theory. Cambridge University Press, 2 edition, 1992. .
4. M V Berry. Focusing and twinkling: critical exponents from catastrophes in non-gaussian random short waves. Journal of Physics A: Mathematical and General, 10(12):2061–2081, dec 1977. . URL https://doi.org/10.1088/0305-4470/10/12/015.
5. DLMF. *NIST Digital Library of Mathematical Functions*. http://dlmf.nist.gov/, Release 1.1.4 of 2022-01-15, 2022. URL https://dlmf.nist.gov/36.6. F. W. J. Olver, A. B. Olde Daalhuis, D. W. Lozier, B. I. Schneider, R. F. Boisvert, C. W. Clark, B. R. Miller, B. V. Saunders, H. S. Cohl, and M. A. McClain, eds.
6. William H Press, Saul A Teukolsky, William T Vetterling, and Brian P Flannery. Numerical recipes 3rd edition: The art of scientific computing. Cambridge university press, 2007.
7. V. I. Arnol'd. Bifurcations of Equilibria, pages 10–38. Springer Berlin Heidelberg, Berlin, Heidelberg, 1994. ISBN 978-3-642-57884-7. . URL https://doi.org/10.1007/978-3-642-57884-7_1.
8. ML Smith, GM Yanega, and A Ruina. Elastic instability model of rapid beak closure in hummingbirds. Journal of theoretical biology, 282(1):41–51, 2011.